Available online at https://link.springer.com/journal/42241
http://www.jhydrodynamics.com
Journal of Hydrodynamics, 2021, 33(1): 93-103
https://doi.org/10.1007/s42241-021-0015-y

Numerical and experimental study of internal solitary wave loads on tension leg platforms *

Xu Wang[1], Ji-fu Zhou[1, 2]
1. *Key Laboratory for Mechanics in Fluid Solid Coupling System, Institute of Mechanics, Chinese Academy of Sciences, Beijing 100190, China*
2. *School of Engineering Sciences, University of Chinese Academy of Sciences, Beijing 100049, China*

(Received June 19, 2019, Revised December 23, 2019, Accepted March 3, 2020, Published online March 5, 2021)

Abstract: With the large-scale density stratified tank and the numerical flume proposed, series of numerical cases in line with the experiments are carried out to investigate the interaction between the tension leg platforms (TLPs) and the internal solitary waves (ISWs). The waveforms, and the loads and the torques on the TLP obtained by the experiments and the simulations agree well with each other. Experimental results show that the amplitudes of the dimensionless horizontal force and torque linearly increase with the dimensionless amplitude, while that of the vertical force increases in a parabolic curve. Besides, the numerical results indicate that the horizontal and vertical forces on the TLP due to the ISWs can be divided into three components, namely, the wave pressure-difference forces, the viscous pressure-difference forces, and the frictional force that is negligible. The wave pressure-difference forces are always the major constituents. However the viscous pressure-difference component is unimportant, it is negligible as compared with the vertical forces.

Key words: Internal solitary waves (ISWs), tension leg platforms (TLPs), wave loads

Introduction

The internal solitary waves (ISWs) with large amplitudes are a common oceanography phenomenon in the stratified density seawater. They are not only an important link in the sea energy cascade, but also an environment factor with a significant impact on the safety of offshore structures. The ISWs are frequently active in many sea areas all over the world, with serious consequences. For instance, in 1990, a sudden strong current accompanied by an internal wave caused a cable breakage in an extended test period in the Liuhua oilfield in the South China Sea[1]. Therefore, the hydrodynamic impacts of the ISWs are an important issue in the regions with a frequent occurrence of the ISWs[2].

As a semi-rigid compliant platform, the buoyancy of a tension leg platform (TLP) is greater than its own gravity, so that the roll, pitch and heave motions are restricted due to the large pre-tensions of the platform. Therefore, a TLP has a better seakeeping capacity even in a bad sea state, offering as a useful equipment for the deep-water oil-gas exploitation. Reasonably assessing the load of the ISWs is a key issue for the design and the application of the TLPs in an active area of the ISWs. The performance of various offshore structures in an ordinary climate, with wind, waves and currents, was extensively studied both experimentally and numerically. Several methods and software were developed to calculate the hydrodynamic loads[3-8]. Nonetheless, there were relatively few studies of the loading mechanism of the ISWs on the floating structures.

In engineering applications, previous researches were mainly focused on cylinder structures, using the Morison formula[9] to calculate the ISW loads[10-14]. However, the geometry of a TLP is much more complicated than a cylinder, which makes it difficult to determine accurately the drag and inertia coefficients in the Morison formula. Thus, it is difficult to directly calculate the ISW load on a TLP by the Morison formula. The laboratory experiments[15] are a reliable

* Project supported by the National Key Research and Development Program of China (Grant No. 2017YFC1404202), the National Natural Science Foundation of China (Grant Nos. 11972352, 11572332) and the Strategic Priority Research Program of the Chinese Academy of Sciences (Grant Nos. XDB22040203, XDA22000000).
Biography: Xu Wang (1985-), Male, Ph. D., Associate Professor
Corresponding author: Xu Wang,
E-mail: wangxu@imech.ac.cn

approach to study the ISW loads. However, the scale effect of the ISW loads is not very clear, the conversion relation between the experimental model and its prototype can not be easily established.

With the development of the computing capability, the computational fluid dynamics (CFD) provides an effective way to simulate the ISW loads and uncover the load components. As a first step, an accurate and controllable numerical flume is developed to study the interaction between the ISWs and the offshore structures. Previous CFD simulations often had no adequate experimental validation under combined conditions of the density stratifications and the ISW amplitudes. In the present paper, combined with the laboratory experiments, a numerical flume is developed to calculate the ISW loads on the TLP. Furthermore, the components and the characteristics of the ISW loads will be discussed.

1. Experimental facility and procedure

Experiments in several cases are carried out in the large-scale density stratified tank (length: 30.00 m, width: 0.60 m, height: 1.20 m) at Shanghai Jiao Tong University (see Fig. 1). Two push plates as the wave producing facility are located at the front end, the experimental model and the measuring equipment are arranged in the intermediate region, and a wedge-shape wave breaker is set up at the rear end of the tank to prevent the solitary waves from reflecting.

The experimental model is shown in Fig. 2. The forces on the TLP during the ISW propagation are measured by a three-component force balance, which is connected to the model and attached to the top of the tank. Before the experiment, an additional weight is introduced to ensure the balance between the gravity and the buoyancy. Then the weights on the model along the horizontal and vertical directions, respectively, are loaded and unloaded for establishing the calibration relationship between the measured electronic signals and the loads. During the experiment, the ISW loads on the model can be calculated from the electronic signals according to the calibration relationship.

The TLP model is built based on the ISSC-TLP platform (in scale 1:225). The scale parameters of the TLP platform prototype and the experimental model are listed in Table 1.

The stratified two-layer fluid in the tank is prepared in the following way. First, the upper-layer fluid is injected until its height is h_1, then the lower-layer fluid is slowly injected from two mushroom-type inlets at the bottom of the tank until the total height is h. Thus the thickness of the lower-layer is $h_2 = h - h_1$.

Unlike the gravity collapse method[16], at the experimental stage, the ISWs are generated using a double-plate (shown in black color in Fig. 1) wave maker, and the procedure is similar to that described

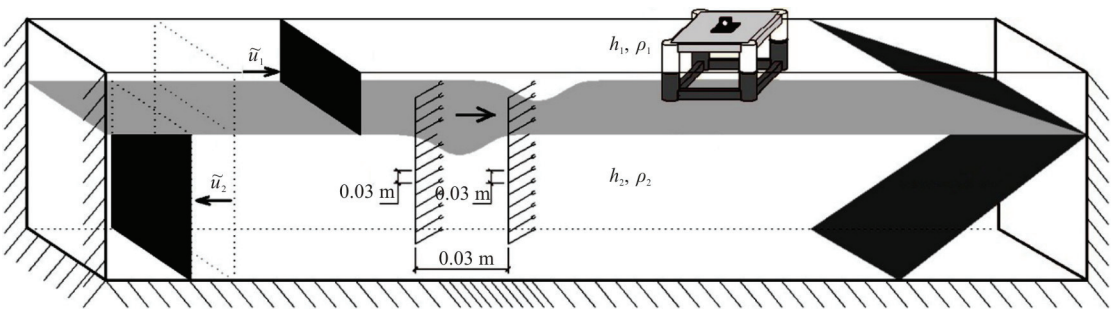

Fig. 1 Principle of internal solitary wave generated by a double-plate wave maker

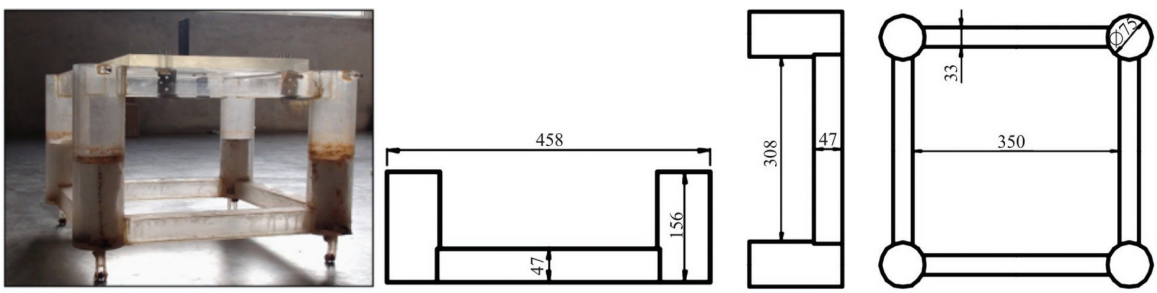

(a) Experimental model (b) The front view (c) The right view (d) The top view

Fig. 2 The submerged model (mm)

Table 1 Parameters for the TLP model and its archetypes

Parameters	Archetypes of TLP platforms	Experimental model
Space of legs/m	86.25	0.383
Radius of legs/m	8.44	0.038
Height of legs/m	76	0.338
Section of caisson/m×m	10.5×7.5	0.047×0.033
Height of gravitational center/m	38	0.169
Draught of Platforms, d /m	35	0.156
Frontal area of the model, S_x /m^2	3 341.25	0.066
Sum of top and bottom area of caisson, S_z /m^2	4 131	0.082
Total mass of platforms/kg	4.05×10^7	3.56

by Wessel and Hutter[17]. In particular, two improvements are made in order to generate nonlinear ISWs with larger amplitudes. First, the drive mechanism of the wave-maker is significantly upgraded and the control software of the two plates is modified. Additionally, a damper plate with a size adjusted through tests is placed on the top of the wave-maker to reduce the disturbance of the free surface.

The two push plates move along in opposite directions at different speeds to generate an ISW at the interface between the two layers. At the preparation stage, the two push plates are set at the same heights as the undisturbed fluid layers (h_1, h_2). During the generation process, the speed of the upper and lower push plates $(\bar{u}_1, \bar{u}_2)$, respectively, is controlled by a computer and can be expressed as:

$$\bar{u}_1 = -c\frac{\zeta(t)}{h_1},\ \bar{u}_2 = c\frac{\zeta(t)}{h_2} \tag{1}$$

where c is the phase speed, $\zeta(t)$ denotes the interface displacement of the desired ISW.

The ISWs are measured using two rows of conductivity probes, arranged at intervals of 0.03 m. Each row includes 13 equally distributed probes, and the distance between the rows is 0.03 m. It is known that the conductivity has a linear relationship with the density variation, so we can easily obtain the ISW interface displacement as well as the phase speed by post-processing the conductivity signal measured by the two rows of probes.

The trailing-wave behind the leading ISW is often unavoidable in the experiment stage. The existence of the trailing waves implies the dissipation of the wave energy during the wave generation. As a result, the measured amplitude is always less than the desired amplitude for the experiment. To generate the desired waveform for a specific case, first we have to find the relation between the measured amplitude a_m and the desired amplitude a_d based on a series of experiments. Then the desired amplitude can be achieved by adjusting the input parameters according to the relation mentioned above.

2. Numerical methods

2.1 *Governing equations*

With the two-layer fluid approximation, a numerical flume (Fig. 3) is built to simulate the nonlinear interactions between the ISWs and a TLP, where the ISWs are obtained by adding a mass source/sink term to the continuity equation. For an incompressible fluid of density, ρ_i, the governing equations can be written as:

$$u_{ix} + v_{iy} + w_{iz} = 0 \tag{2}$$

$$u_{it} + u_i u_{ix} + v_i u_{iy} + w_i u_{iz} = \frac{-p_i}{\rho_i} + \nu(u_{ixx} + u_{iyy} + u_{izz}) \tag{3}$$

$$v_{it} + u_i v_{ix} + v_i v_{iy} + w_i v_{iz} = \frac{-p_i}{\rho_i} + \nu(v_{ixx} + v_{iyy} + v_{izz}) \tag{4}$$

$$w_{it} + u_i w_{ix} + v_i w_{iy} + w_i w_{iz} = \frac{-p_i}{\rho_i} + \nu(w_{ixx} + w_{iyy} + w_{izz}) - g \tag{5}$$

where (u_i, v_i, w_i) are the velocity components in Cartesian coordinates, p_i is the pressure and ν is the dynamic viscosity. Note that the subscripts with

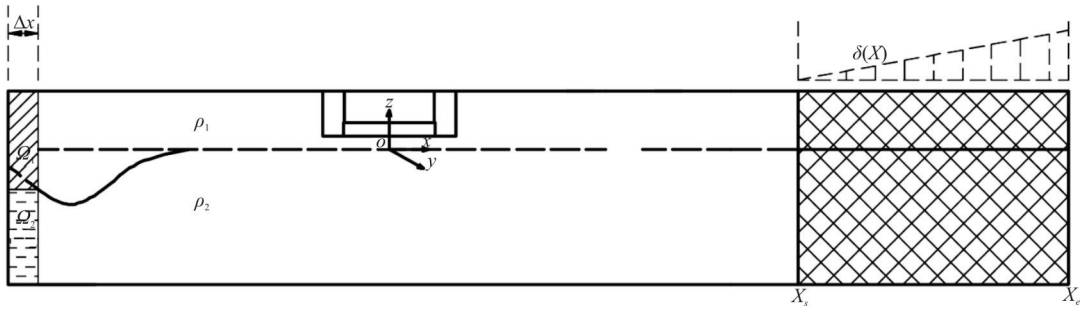

Fig. 3 The front view of the 3-D computation domain

respect to space and time represent partial differentiations, and $i=1(i=2)$ denotes the upper (lower) layer fluid. g is the gravitational acceleration.

The additional mass source term $S_i(x,y,z,t)$ in Eq. (1) is a nonzero function only in the source region Ω. Bordered by the ISW interface, the source region can be divided into two subregions: Ω_1 and Ω_2, which are the source region and the sink region, respectively. The source/sink term $S_i(t)$ was proposed in Ref. [18]:

$$S_1(t)=-\rho_1 c\frac{\zeta(t)}{h_1-\zeta(t)}\frac{1}{\Delta x},\ S_2(t)=\rho_2 c\frac{\zeta(t)}{h_2+\zeta(t)}\frac{1}{\Delta x} \tag{6}$$

where c denotes the phase speed, Δx is the width of the mass source region, and $\zeta(t)$ is the interface displacement of the ISW.

2.2 *Boundary and initial conditions*

The volume of fluid (VOF) method[19] is employed to track the ISW interface $z=\zeta(x,y,t)$. At the interface, the normal velocity is continuous, so is the pressure.

$$\zeta_t+u_1\zeta_x+v_1\zeta_y=w_1,\ \zeta_t+u_2\zeta_x+v_2\zeta_y=w_2,\ p_1=p_2 \tag{7}$$

At the top and the bottom of the fluid domain, the rigid-lid approximation is adopted:

$$w_1\big|_{z=h_1}=0,\ w_2\big|_{z=-h_2}=0 \tag{8}$$

Moreover, the surface of the platform is set as an impermeability boundary, and the forces and the torque on the surface are monitored during the simulation.

A symmetry condition is imposed on the left boundary in the source term wave-generation method. The sidewalls and the right end boundary are specified as non-slip walls. In order to avoid the wave reflection at the end, a buffering region is allocated to dissipate the ISWs in the numerical flume, realized by adding a source term to the momentum equation in the vertical direction

$$w_{it}+u_iw_{ix}+v_iw_{iy}+w_iw_{iz}=\frac{-p_i}{\rho_i}+\nu(w_{ixx}+w_{iyy}+w_{izz})-g-\delta(x)w \tag{9}$$

where the damping function $\delta(x)$ is nonzero only in the dissipation region, otherwise $\delta(x)=0$. In the present paper, we choose $\delta(x)$ as a linear function

$$\delta(x)=C_s\frac{x-x_s}{x_e-x_s} \tag{10}$$

where C_s is an empirical coefficient depending on the specific case, while x_s and x_e respectively, denote the horizontal coordinates of two endpoints of the dissipation region $(x_s<x_e)$.

The still water with no wave or current motions is assumed as the initial condition.

2.3 *Forces and their components*

The horizontal force F_x, the vertical force F_z and the torque M_y are measured by the three-component force balance at the experiment stage and monitored during the simulation. The lateral force F_y (caused by a periodic trailing vortex behind the TLP) is much weaker than F_x or F_z, so it is not discussed in the paper. F_x, F_z and M_y on a TLP can be expressed as:

$$F_x=\mu\int_s\left[\left(\frac{\partial u}{\partial y}+\frac{\partial v}{\partial x}\right)n_y+\left(\frac{\partial u}{\partial z}+\frac{\partial w}{\partial x}\right)n_z\right]\mathrm{d}s-\int_s pn_x\mathrm{d}s \tag{11}$$

$$F_z = \mu \int_s \left[\left(\frac{\partial u}{\partial z} + \frac{\partial w}{\partial x} \right) n_x + \left(\frac{\partial v}{\partial z} + \frac{\partial w}{\partial y} \right) n_y \right] \mathrm{d}s - \int_s p n_z \mathrm{d}s \tag{12}$$

$$M_y = \mu \int_s \left[\left(\frac{\partial u}{\partial y} + \frac{\partial v}{\partial x} \right) n_y + \left(\frac{\partial u}{\partial z} + \frac{\partial w}{\partial x} \right) n_z \right] d\mathrm{d}s - \int_s p n_x d\mathrm{d}s \tag{13}$$

where μ denotes the dynamic viscosity of the water (1.01×10^{-3} N·s/m^2), s is the wetted surface of the TLP, and (n_x, n_y, n_z) is the outward unit normal vector of the surface, d is the arm of the horizontal force of each wetted cell of the structure, namely, the vertical distance between the cell center and the moment center. In the formulas (11) and (12), the forces are represented by two parts, the first term is the friction (f_x, f_z) and the second one is the pressure-difference force (F_x^p, F_z^p).

$$F_x^p = -\int_s p n_x \mathrm{d}s \tag{14}$$

$$F_z^p = -\int_s p n_z \mathrm{d}s \tag{15}$$

$$f_x = \mu \int_s \left[\left(\frac{\partial u}{\partial y} + \frac{\partial v}{\partial x} \right) n_y + \left(\frac{\partial u}{\partial z} + \frac{\partial w}{\partial x} \right) n_z \right] \mathrm{d}s \tag{16}$$

$$f_z = \mu \int_s \left[\left(\frac{\partial u}{\partial z} + \frac{\partial w}{\partial x} \right) n_x + \left(\frac{\partial v}{\partial z} + \frac{\partial w}{\partial y} \right) n_y \right] \mathrm{d}s \tag{17}$$

Furthermore, to study the constituents of the load, according to the contribution of the viscosity, the pressure-difference force can be divided into two components: the wave pressure-difference force (F_x^{pw}, F_z^{pw}) and the viscous pressure-difference force (F_x^{pv}, F_z^{pv}). The wave pressure-difference force is associated with the fluctuation of the water parcels, which can be calculated based on the Euler equations, while the viscous pressure-difference force is associated with the viscous effect, which can be calculated by subtracting the wave pressure-difference force obtained by the Euler equations from that obtained by the Navier-Stokes (N-S) equations. The expressions of (F_x^{pw}, F_z^{pw}) and (F_x^{pv}, F_z^{pv}) are as follows:

$$F_x^{pw} = -\int_s p n_x \mathrm{d}s_{\text{(Euler)}} \tag{18}$$

$$F_z^{pw} = -\int_s p n_z \mathrm{d}s_{\text{(Euler)}} \tag{19}$$

$$F_x^{pv} = -\int_s p n_x \mathrm{d}s_{\text{(N-S)}} + \int_s p n_x \mathrm{d}s_{\text{(Euler)}} \tag{20}$$

$$F_z^{pv} = -\int_s p n_z \mathrm{d}s_{\text{(N-S)}} + \int_s p n_z ds_{\text{(Euler)}} \tag{21}$$

2.4 *Numerical implementation*

In line with the experimental configuration, the length of the numerical flume is 30 m (in which $\Delta x = 0.04$ m and the width of the damping region is 6 m, the total depth is 1 m. The upper layer fluid density ρ_1 is 998 kg/m^3, and the lower layer fluid density ρ_2 is 1 025 kg/m^3. In addition, the parameters of the TLP model in the simulation are listed in Table 1.

With the numerical model, the calculation proceeds as follows: first the ISW interface displacement $\zeta(t)$ is calculated, substituted in the mass source function given by Eq. (6), and the ISW is excited in the source term region. During the propagation of the ISW, the forces on the TLP are monitored in real time. It should be noted that although the numerical simulation is carried out with the user defined function (UDF) tools on the platform of the Fluent software, it is also applicable to other calculation platforms.

The governing equations are discretized by three-dimensional structured grids using a finite volume method (FVM) and some numerical schemes are adopted to avoid spurious effects. In addition, the structured elements are used to ensure the mesh quality in the computational domain. Particularly, the local grids are refined to reduce the numerical dispersion around the TLP model (as shown in Fig. 4), while sparse grids are employed in the buffering region to ease the computational burden. A time step of $\Delta t = 0.005$ s is used in the simulation.

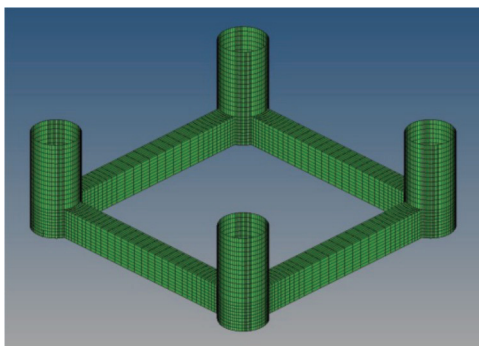

Fig. 4 (Color online) The grid distribution for the wet surface of the TLP

3. Experimental and numerical results

According to the roles played by the nonlinearity and the dispersion in the propagation of the ISWs[20], the ISWs can be commonly described by the Korteweg-de Vries (KdV) equation, the extended KdV (eKdV) equation, the Miyata-Choi-Camassa (MCC) equation and others[21-22]. In order to validate the numerical method for different ISW theories, in the present paper, 15 numerical and experimental cases with different depths and wave amplitudes are analyzed (Table 2).

Table 2 The numerical experiments under the action of the ISWs and the platforms

ID	h_1 / m	h_2 / m	a_d / m	ISW theory
A1	0.20	0.80	0.048	KdV
A2	0.20	0.80	0.105	eKdV
A3	0.20	0.80	0.124	eKdV
A4	0.20	0.80	0.144	eKdV
A5	0.20	0.80	0.193	eKdV
B1	0.25	0.75	0.056	KdV
B2	0.25	0.75	0.081	eKdV
B3	0.25	0.75	0.115	eKdV
B4	0.25	0.75	0.137	eKdV
B5	0.25	0.75	0.156	eKdV
C1	0.30	0.70	0.049	KdV
C2	0.30	0.70	0.079	eKdV
C3	0.30	0.70	0.103	eKdV
C4	0.30	0.70	0.121	eKdV
C5	0.30	0.70	0.136	MCC

3.1 V*alidation of the numerical model*

Figure 5 shows the comparisons of the wave profiles of the ISWs between the CFD simulations, the theories and the laboratory experiments. As shown in Table 2, cases B1, A4 and C5 represent the weakly, moderately and strongly nonlinear ISWs, respectively. Both the numerical and experimental waveforms are in good agreement with the theoretical results (the relative errors are within 3%), which indicates that the experimental wave-maker and the numerical approaches can accurately generate the waveform in the presence of the TLP, no matter it is a weakly or a strongly nonlinear ISW.

In the present paper, we define $\overline{F_x} = F_x/(\rho_1 g S_x d)$, $\overline{F_z} = F_z/(\rho_1 g S_z^{3/2})$ and $\overline{M_y} = M_y/(\rho_1 g S_x^2)$ (where S_x, S_z, d are defined in Table 1) as the dimensionless horizontal, vertical forces, and torque on the TLP due to the ISWs, respectively. The amplitudes of the dimensionless loads and torques are shown in Fig. 6, demonstrating that the amplitudes of the horizontal and vertical forces, as well as the torque obtained numerically are in good agreement with the experimental results, with the maximum error less than 11%. The maximum error often shows up in the later stage (for example, cases B4, B5) for each density stratification setting. One possible reason is the deviation of the density structure from the strict two-layer configuration after several rounds of experiments.

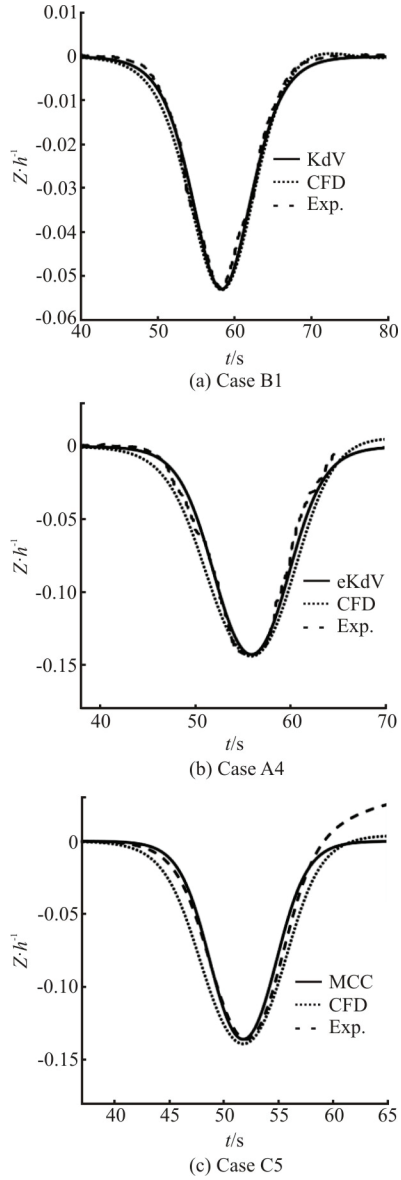

Fig. 5 Comparisons of profiles of ISWs (Note that the scales are different in the three panels)

Figutre 7 shows the time variations of the dimensionless loads and torque for case A4. The numerical and experimental results are in good agreement, which means that it is reasonable and feasible to calculate the loads and the torque on the TLP based on the proposed numerical flume. According to Eq. (13), the torque $\overline{M_y}$ is proportional to the horizontal load $\overline{F_x}$. Hence, we primarily focus on $\overline{F_x}$ and $\overline{F_z}$ in the subsequent analyses.

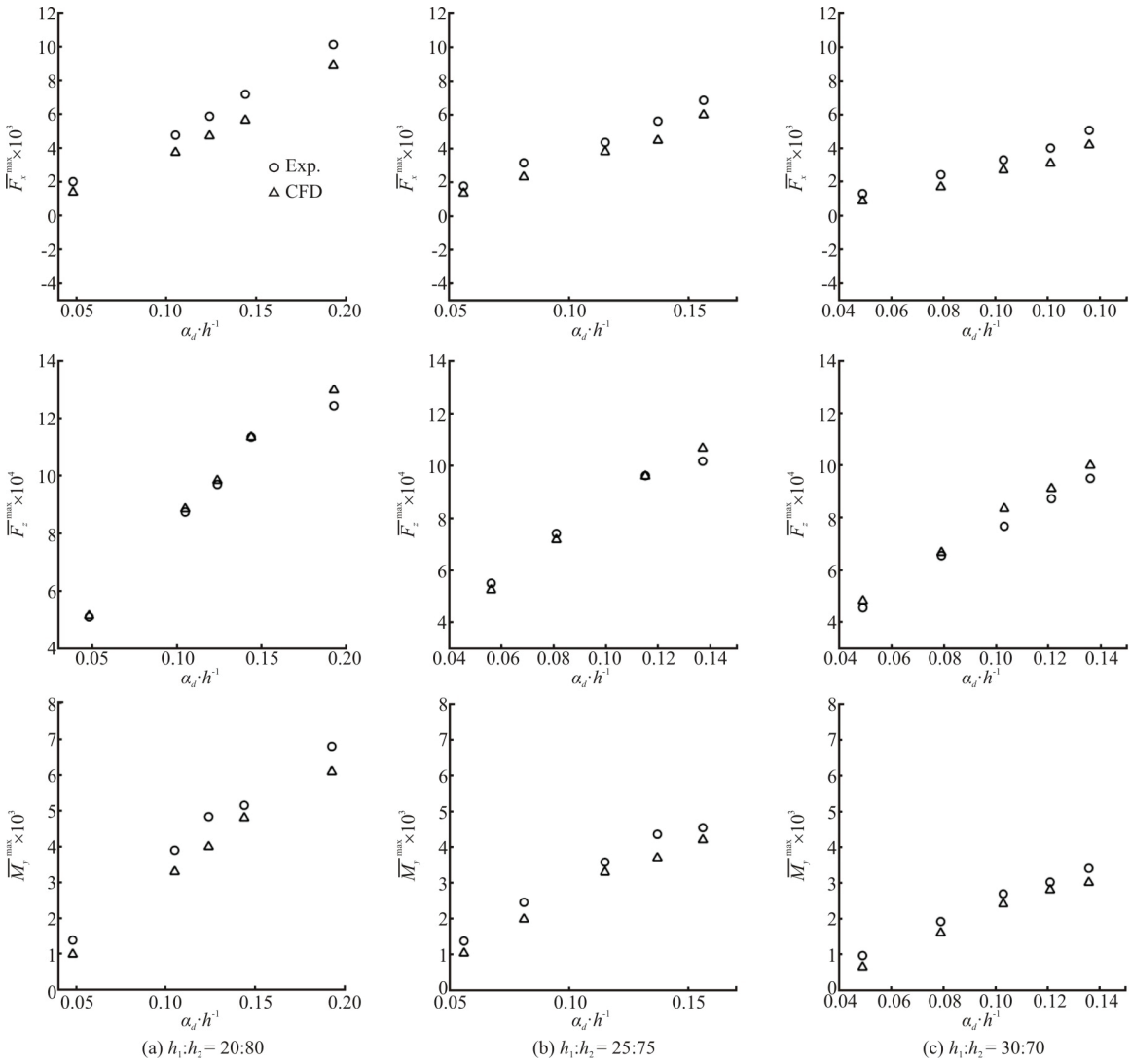

Fig. 6 The numerical and experimental amplitudes of dimensionless loads $(\overline{F_x}, \overline{F_z})$ and torques $\overline{M_y}$

In order to verify the grid and time step independence, two different grid distribution cases (Table 3) and two different time step cases (Table 4) are considered in case A4. The simulated maximum loads $(\overline{F_x}^{\max}, \overline{F_z}^{\max})$ are listed. It is seen that a more refined grid and a smaller time step than the originally used ones do not improve the precision significantly, which indicates that the numerical results with the current grid distribution and time step are stable and convergent for case A.

3.2 *The relationship between ISW loads and ISW amplitudes*

Figure 8 presents the experimental dimensionless amplitudes of the loads and the torque versus the dimensionless ISW amplitudes for the cases of different depth ratios. In Fig. 8(a) the dimensionless horizontal force increases approximately linearly with the amplitude, while the line slope decreases with the increase of the depth ratio (h_1 / h_2). By means of the regression analysis, the lines can be expressed in the following formulas:

$$\overline{F_x}^{\max} = k_x \frac{|a_d|}{h_1 + h_2}, \quad k_x = -0.16\left(\frac{h_1}{h_1 + h_2}\right) + 0.0815 \tag{22}$$

Unlike the horizontal forces in Fig. 8(a), the amplitudes of the vertical force increase along a parabolic curve (see Fig. 8(b)). Similarly, the vertical

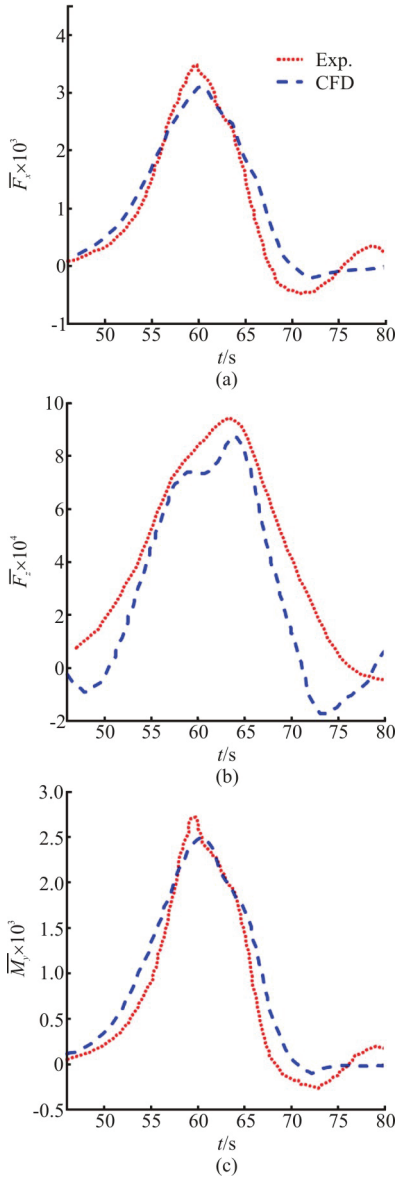

Fig. 7 (Color online) Time variations of dimensionless loads and torque for case A4 (Note that the scales are different in the three panels)

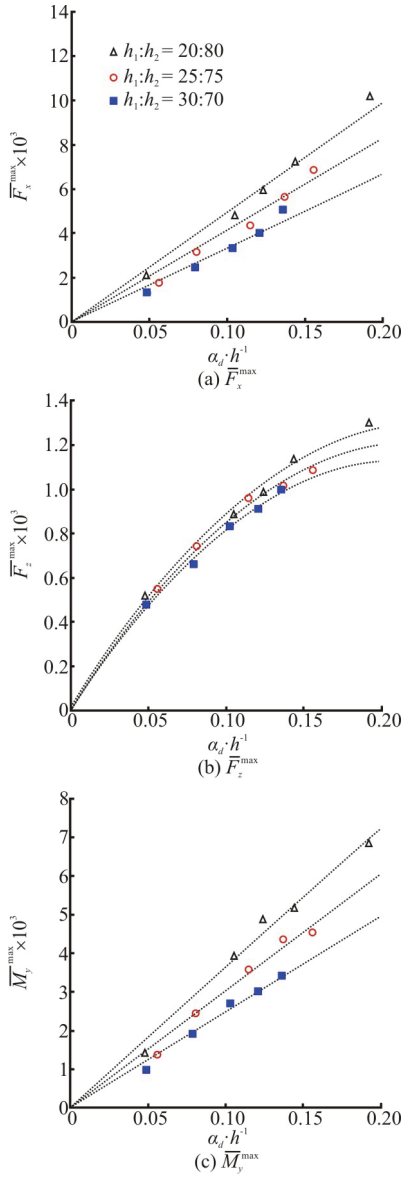

Fig. 8 (Color online) The experimental amplitudes of dimensionless loads versus $a_d/(h_1+h_2)$

Table 3 The numerical results for the grid-independence test (iteration step: 0.005 s)

ID	Grid quantity	$\overline{F_x}^{\max}$	$\overline{F_z}^{\max}$
Case A4	1 769 477	3.10×10^{-3}	8.73×10^{-4}
Case A4-grid test 1	2 587 454	3.10×10^{-3}	8.76×10^{-4}
Case A4-grid test 2	4 087 973	3.10×10^{-3}	8.76×10^{-4}

Table 4 The numerical results for the time step-independence test (grid number: 1 769 477)

ID	Time step	$\overline{F_x}^{\max}$	$\overline{F_z}^{\max}$
Case A4	0.005	3.10×10^{-3}	8.73×10^{-4}
Case A4-grid test 1	0.002	3.10×10^{-3}	8.75×10^{-4}
Case A4-grid test 2	0.001	3.10×10^{-3}	8.75×10^{-4}

force amplitudes increase with the decrease of the depth ratio. The quadratic curves can be fitted as:

$$\overline{F_z}^{\max} = -0.0251\left(\frac{|a_d|}{h_1+h_2}\right)^2 + k_z\frac{|a_d|}{h_1+h_2},$$

$$k_z = -0.0075\left(\frac{h_1}{h_1+h_2}\right) + 0.0129 \tag{23}$$

Similar to the variation of the horizontal forces, the linear regression relation for the torque amplitudes $\overline{M_y}^{\max}$ can be expressed as (see Fig. 8(c)):

$$\overline{M_y}^{\max} = k_y \frac{|a_d|}{h_1 + h_2}, \quad k_y = -0.1128\left(\frac{h_1}{h_1 + h_2}\right) + 0.0586 \tag{24}$$

3.3 *The components of ISW loads*

Now, let us discuss the components of the ISW loads in terms of the viscosity effects. Firstly, it is necessary to analyze the influence of the fluid viscosity on the generation and the propagation of the ISWs. Two simulations based on the Navier-Stokes equations and the Euler equations are carried out. The wave profiles for Case A4 simulated by the two systems are shown in Fig. 9. Results show that the waveforms generated by the two different simulation methods are stable with only a slight differences, indicating that the influence of the fluid viscosity on the ISW propagation is slight.

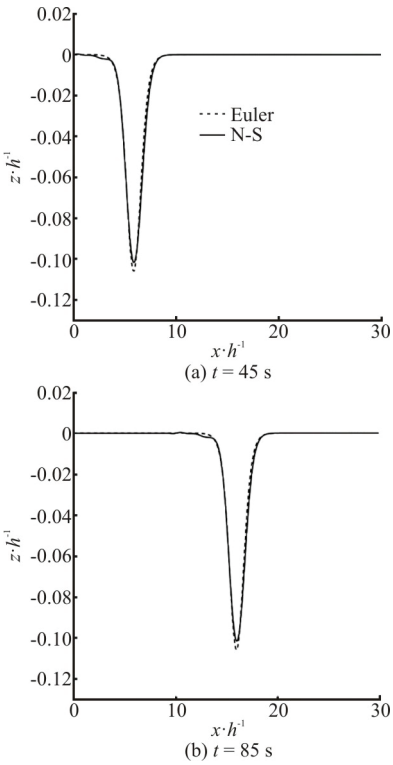

Fig. 9 The numerical results for the ISW waveforms with two different simulation methods for case A4

It can be seen From Eqs.(11) and (12) that both the horizontal and vertical forces have two components, related to the pressure-difference and the friction, respectively. The time variations of these two components for case A4 are shown in Fig. 10. The results indicate that the pressure-difference forces (F_x^p, F_z^p) are the dominant component, while the friction forces (f_x, f_z) re ignorable.

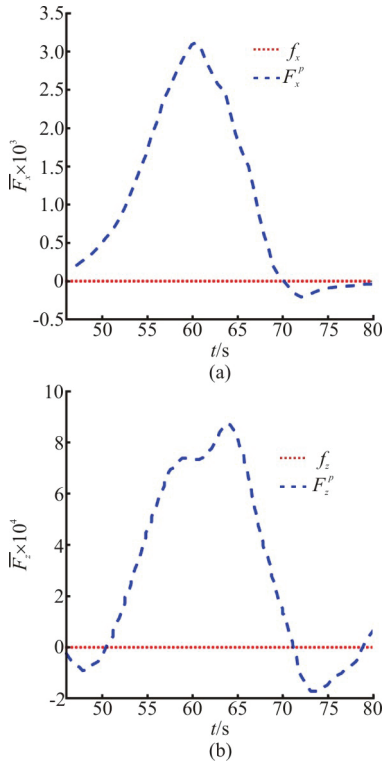

Fig. 10 (Color online) Time variations of the pressure-difference and friction forces for case A4 (Note that the scales are different in the two panels)

The time variations of the wave and the viscous pressure-difference forces due to the ISWs for case A4 are shown in Fig. 11. For the horizontal force, the viscous effect is small but cannot be ignored (the absolute maximum of (F_x^{pw}, F_x^{pv}) is (2.6×10^{-3}, 5.8×10^{-4})), whereas for the vertical force, the viscous pressure-difference force is negligible (the absolute maximum of (F_z^{pw}, F_z^{pv}) is (9.2×10^{-4}, 7.7×10^{-6})).

4. Conclusions

Combined with the laboratory experiments, a numerical model based on the N-S equations is used to simulate the nonlinear interactions between the ISWs and a TLP platform, where the ISWs are generated by adding a mass source term and a sink term to the continuity equation in the source region located within the computational domain. The variations of the ISW loads against the depth ratio and the contributions of each component to the total ISW loads are discussed in detail. The conclusions are as follows:

(1) In the presence of the platforms, the waveform and the ISW loads/torque obtained by the proposed numerical model are in good agreement with the experimental results. Hence, the numerical model

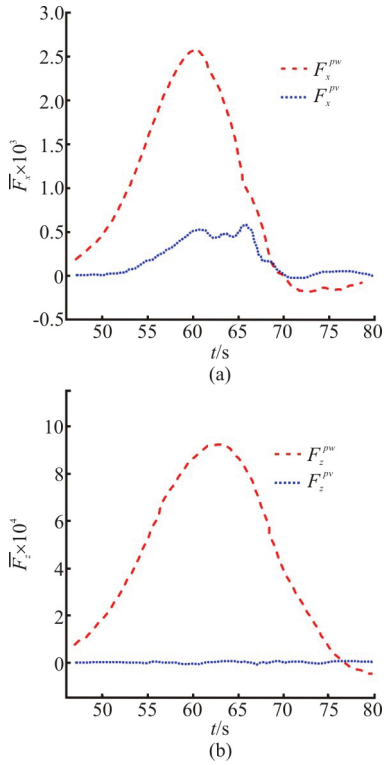

Fig. 11 (Color online) Time variations of wave pressure-difference force (dashed curve) and viscous pressure-difference force (dotted curves) for case A4 (Note that the scales are different in the two panels)

is capable of simulating the nonlinear interactions between the ISWs and the TLP platforms.

(2) The amplitudes of the experimental dimensionless ISW horizontal force and torque linearly increase with the dimensionless ISW amplitude, while those of the vertical force increase in a parabolic curve. The gradients of the regression lines of the experimental forces/ torque have a negative correlation with the depth ratio, implying that the increasing rate of the ISW loads with the ISW amplitude decreases with the depth ratio.

(3) In terms of the load components, the hydrodynamic force on a TLP consists of three components: the wave and viscous pressure-difference components, and the friction component. Specifically the friction component is shown to be very small and can be neglected. The wave pressure-difference forces are the major constituents both for the horizontal and the vertical forces. However, the viscous pressure-difference component is unimportant, it can be neglected as compared with the vertical forces.

(4) The present studies are carried out in the laboratory scale (low Reynolds number), not all conclusions can be directly extrapolated to the prototype size due to the unclear scale effect. The scale effect of the ISW loads on the TLP platfroms will be investigated in the future.

References

[1] Bole J., Ebbesmeyer C., Romea R. Soliton currents in the South China Sea: measurements and theoretical modeling [C]. *Offshore Technology Conference*, Houston, USA, 1994.

[2] Tan D. L., Zhou J. F., Wang X. Fission law of solitary waves propagating over sharply variable topography[J]. *Journal of Hydrodynamics*, 2020, 32(4): 727-734.

[3] Male P. V. D., Vergassola M., Dalen K. N. V. Decoupled modelling approaches for environmental interactions with monopile-based offshore wind support structures [J]. *Energies*, 2020, 13(19): 5195.

[4] Kvittem M. I., Bachynski E. E., Moan T. Effects of hydro-dynamic modelling in fully coupled simulations of a semi-submersible wind turbine [J]. *Energy Procedia*, 2012, 24: 351-362.

[5] Xu W. H., Zeng X. H., Wu Y. X. et al. Hill instability analysis of TLP tether subjected to combined platform surge and heave motions [J]. *China Ocean Engineering*, 2008, 22(4): 533-546.

[6] Söylemez M., Yilmaz O. Hydrodynamic design of a TLP type offloading platform [J]. *Ocean Engineering*, 2003, 30(10): 1269-1282.

[7] Suja-Thauvin L., Bachynski E. E., Pierella F. et al. Critical assessment of hydrodynamic load models for a monopile structure in finite water depth [J]. *Marine Structures*, 2020, 72: 102743.

[8] Wu X., Hu Y., Li Y. et al. Foundations of offshore wind turbines: A review [J]. *Renewable and Sustainable Energy Reviews*, 2019, 10(4): 379-393.

[9] Wang J. S., Fan D., Lin K. A review on flow-induced vibration of offshore circular cylinders [J]. *Journal of Hydrodynamics*, 2020, 32(5): 415-440.

[10] Cai S., Long X., Gan Z. A method to estimate the forces exerted by internal solitons on cylindrical piles [J]. *Ocean Engineering*, 2003, 30(5): 673-689.

[11] Cai S., Long X., Wang S. Forces and torques exerted by internal solitons in shear flows on cylindrical piles [J]. *Applied Ocean Research*, 2008, 30(1): 72-77.

[12] Cai S., Wang S., Long X. A simple estimation of the force exerted by internal solitons on cylindrical piles [J]. *Ocean Engineering*, 2006, 33(7): 974-980.

[13] Si Z., Zhang Y., Fan Z. A numerical simulation of shear forces and torques exerted by large-amplitude internal solitary waves on a rigid pile in South China Sea [J]. *Applied Ocean Research*, 2012, 37: 127-132.

[14] Song Z. J., Teng B., Gou Y. et al. Comparisons of internal solitary wave and surface wave actions on marine structures and their responses [J]. *Applied Ocean Research*, 2011, 33(2): 120-129.

[15] Huang W H., You Y. X., Wang J. Y. et al. Internal solitary wave loads and its theoretical model for a tension leg platform [J]. *Journal of Shanghai Jiaotong University (Science)*, 2013, 47(10): 1494-1502(in Chinese).

[16] Du H., Wei G., Gu M. et al. Experimental investigation of the load exerted by nonstationary internal solitary waves on a submerged slender body over a slope [J]. *Applied Ocean Research*, 2016, 59: 216-223.

[17] Wessels F., Hutter K. Interaction of internal waves with a topographic sill in a two-layered fluid [J]. *Journal of Physical Oceanography*, 1996, 26(1): 5-20.

[18] Wang X., Zhou J., You Y. A numerical wave-maker for internal solitary waves with timely updated mass source/sink terms [J]. *European Journal of Mechanics-B/Fluids*, 2017, 65: 274-283.

[19] Paz C., Suárez E., Vence J. et al. Analysis of the volume of fluid (VOF) method for the simulation of the mucus clearance process with CFD [J]. *Computer Methods in Biomechanics and Biomedical eEgineering*, 2019, 22(5): 547-566.

[20] Camassa R., Choi W., Michallet H. et al. On the realm of validity of strongly nonlinear asymptotic approximations for internal waves [J]. *Journal of Fluid Mechanics*, 2006, 549: 1-23.

[21] Choi W., Camassa R. Weakly nonlinear internal waves in a two-fluid system [J]. *Journal of Fluid Mechanics*, 1996, 313: 83-103.

[22] Helfrich K. R., Melville W. K. Long nonlinear internal waves [J]. *Annual Review of Fluid Mechanics*, 2006, 38: 395-425.